Pergamon

Int. J. Heat Mass Transfer. Vol. 39, No. 10, pp. 2115–2130, 1996

0017-9310/96 $15.00 + 0.00

0017-9310(95)00313-4

Radiation–conduction interaction: an investigation on silica aerogels

U. HEINEMANN and R. CAPS

Bavarian Center of Applied Energy Research—ZAE Bayern, Am Hubland, D-97074 Würzburg, Germany

and

J. FRICKE†

Physikalisches Institut der Universität Würzburg, Am Hubland, D-97074 Würzburg, Germany

(*Received* 10 *March* 1995 *and in final form* 20 *July* 1995)

Abstract—Thermal transport in low density silica aerogels was studied theoretically and experimentally over a wide range of optical thickness and ratio of radiative to conductive heat transfer. Measurements on the combined heat transfer were performed for aerogel densities between 5 and 220 kg m^{-3}, for temperatures from 100 to 650 K, for internal gas pressures between 10^{-4} and 1000 hPa and two boundary emissivities of 0.04 and 0.77. A high precision numerical method for the calculation of the temperature profile and the total (combined) heat flux in these semi-transparent, non-scattering, non-grey media is presented. Copyright © 1996 Elsevier Science Ltd.

1. INTRODUCTION

Silica aerogels consist of highly porous SiO_2 with pore diameters generally below 100 nm [1]. As the mean free path of gas molecules at ambient pressure is in the same range, gas conductivity is not fully developed at 1000 hPa gas pressure and can be suppressed by evacuation to pressures of only 100 hPa (at an aerogel density of 100 kg m^{-3}). Due to the low density (5–300 kg m^{-3}), heat transfer by solid conduction is rather small [2]. As the pore sizes are smaller than the wavelengths of visible light, most aerogels are transparent for visible light. The transparency combined with a high thermal resistance makes aerogels attractive for special applications: as load bearing, evacuated spacers between glass panes for highly insulating windows, as a filler medium between absorber and cover glass in evacuated solar collectors or as granular material in transparent insulation systems for house walls or in daylighting applications.

Heat transfer in aerogels occurs by three mechanisms: solid conduction via the SiO_2 skeleton, gaseous conduction in the pores (which may be eliminated or reduced by evacuation) and thermal radiation.

Due to the small density, solid conductivity λ_{sc} via the skeleton in evacuated samples is very low ($\leqslant 0.01$ W m^{-1} K^{-1}. The solid conductivity λ_{sc} scales with density according to $\lambda_{sc} \propto \rho^{\alpha}$, with $\alpha \approx 1 \ldots 2$ [3–5].

As the pore sizes are much smaller than the wavelengths of the infrared (IR) photons, the extinction of heat radiation is only caused by absorption and not by scattering. In these 'diluted glasses' the extinction coefficient $E(\Lambda)$, which is strongly wavelength dependent, is proportional to the density ρ: $E(\Lambda) = e(\Lambda) \cdot \rho$, with $e(\Lambda)$ = specific extinction.

According to the above relations the ratio of heat transfer by radiation to the heat transfer by solid conduction varies approximately inversely with the second to the third power of density ρ. Due to their low density, radiation is an important or even the dominant heat transfer mechanism in aerogels, even at ambient temperature. Thus the interaction of radiation with conduction in semitransparent media, a phenomenon which becomes of technical importance in glass melts in furnaces or in gases in combustion chambers at high temperatures, may be studied in aerogels experimentally even at room temperatures.

We performed thermal heat loss measurements on a wide variation of the aerogel density, temperature and internal gas pressure and compared the results with a theoretical model of the heat transfer in semi-transparent media. For the experimental, as well as for the numerical, investigations of the combined heat transfer we chose a semi-transparent non-scattering planar aerogel layer covered by grey diffusely emitting and reflecting surfaces.

Measurements of the total (combined) heat transfer were performed at temperatures up to 400°C. The

† Author to whom correspondence should be addressed.

NOMENCLATURE

A	absorption coefficient
D	pore size
E	extinction coefficient
E_n	exponential integral
T	temperature
T_{rad}	mean temperature for radiation
c_p	specific heat
d	sample thickness
e	mass specific extinction
$f_{0-\Lambda T}$	fractional function of the 1st kind
$f^*_{\Lambda T}$	fractional function of the 2nd kind
i	radiation intensity
i_b	blackbody emission
k	heat transfer coefficient
l	mean free path
n	index of refraction
p	pressure
q	heat flux
s	radiation path
t	time
x	spatial coordinate.

Greek symbols

Λ	vacuum wavelength
α	scaling exponent
β	constant in equation (12)
ε	emissivity of surfaces
σ	Stefan–Boltzmann constant
θ	angle of incidence
λ	thermal conductivity
$\lambda_{gas,0}$	conductivity of the free gas
μ	$\cos\theta$
ν	frequency
ρ	density
τ	optical path/depth
τ_0	optical thickness.

Subscripts

ν, Λ	spectral dependent properties
1, 2	properties of the boundaries
cond	(solid and gaseous) conduction
sc	solid conduction
gas	property of the gas
rad	radiation
tot	total
k	index for the spectral bands
i, j	indices for discrete spatial coordinates
n	index for discrete steps in time.

Superscripts

+	in forward direction
−	in backward direction
*	apparent property or parameter for integration.

relevant infrared extinction data, needed as input for the numerical calculations, were measured with a FT-infrared spectrometer.

In the experiment the ratio of radiative to conductive heat transfer, which is an important parameter for the theoretical model, has been varied over several orders of magnitude:

(i) by investigation of several samples of different density (5–220 kg m^{-3});
(ii) by varying the mean temperature from 100 to 670 K;
(iii) by varying the gaseous conduction without influencing the radiative properties by changing the gas pressure (10^{-4} to 1000 hPa).

As is known from silica glass, the spectral absorption in aerogels varies over four orders of magnitude. Thus the shift of the maximum of blackbody emission towards shorter wavelengths with temperature causes an additional variation of effective optical thickness from optical thick at lower temperatures to semi-transparent or transparent at elevated temperatures.

Previous theoretical work on combined heat transfer in one-dimensional systems has been done on semi-transparent grey media [6–9] and on simplified non-grey media, mostly described by two bands [8–12]. Beyond these publications the numerical method in this work had to take into account the very large variation of IR-optical properties with wavelength and density (over six orders of magnitude) and has to give reliable results for any ratio of radiation to conduction in order to meet the investigated system.

In the first part of this paper the theoretical model and the numerical method are presented. High precision numerical results are compared with data from simplified systems, reported earlier by other authors. Then the results of the experimental investigations, IR-optical measurements as well as heat transfer measurements, are presented. These are compared with numerical results.

2. THEORETICAL ANALYSIS

2.1. *Mathematical formulation*

We consider a flat layer of homogeneous, isotropical, non-scattering, non-convecting medium of thickness d between two diffusively emitting and reflecting surfaces at temperatures T_1 and T_2 ($T_1 > T_2$) (see Fig. 1). The boundaries are opaque and are in contact with the adjacent medium. In the interval $[T_1, T_2]$ solid and gaseous conductivity λ_{sc} and λ_{gas}, as well as the IR-optical properties, n_ν and E_ν are treated to be temperature independent (here $E_\nu = A_\nu$, as only absorption occurs).

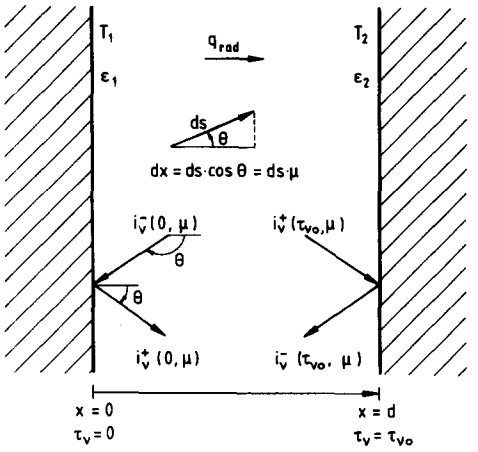

Fig. 1. Physical model.

In general the governing equations are

$$\rho c_p \frac{dT}{dt} = -\frac{d}{dx}(q_{cond} + q_{rad}), \tag{1}$$

with

$$q_{cond} = -\lambda_{cond}\frac{dT}{dx} = -(\lambda_{sc} + \lambda_{gas})\frac{dT}{dx} \tag{2}$$

and

$$q_{rad} = \int_0^\infty q_{rad,\nu}\, d\nu$$

$$= 2\pi \int_0^\infty \int_0^1 [i_\nu^+(x,\mu) - i_\nu^-(x,-\mu)]\mu\, d\mu\, d\nu, \tag{3}$$

where $i_\nu^+(x,\mu)$ and $i_\nu^-(x,-\mu)$ with $(0 < \mu \leqslant 1)$ are the spectral intensities in the forward and the backward directions, respectively, at location x. With the definition of the optical depth along the x-axis $\{\tau_\nu(s) := \rho_\nu(x)/\mu\}$ and the optical thickness of the investigated system $(\tau_{\nu 0} := E_\nu d)$ the spectral intensities are described by the equation of transfer in the integrated form [14]

$$i_\nu^+(\tau_\nu,\mu) = i_\nu^+(0,\mu)e^{-\tau_\nu/\mu} + \int_0^{\tau_\nu} n_\nu^2 i_{b\nu}(T(\tau_\nu^*))e^{-(\tau_\nu-\tau_\nu^*)/\mu}\frac{d\tau_\nu^*}{\mu},$$

$$i_\nu^-(\tau_\nu,-\mu) = i_\nu^-(\tau_{\nu 0},-\mu)e^{-(\tau_{\nu 0}-\tau_\nu)/\mu} + \int_{\tau_\nu}^{\tau_{\nu 0}} n_\nu^2 i_{b\nu}(T(\tau_\nu^*))e^{-(\tau_\nu^*-\tau_\nu)/\mu}\frac{d\tau_\nu^*}{\mu}. \tag{4}$$

For a given temperature profile $T(x = \tau_\nu/E_\nu)$ the spectral intensities at the surfaces $i_\nu^+(0,\mu)$ and $i_\nu^-(\tau_{\nu 0},-\mu)$ are defined by the boundary conditions. For opaque grey diffusely reflecting and emitting surfaces with emissivities ε_1, ε_2 and temperatures T_1, T_2 they are independent of direction μ and can be derived as [13, 14]

$$i_\nu^+(0) = \frac{n_\nu^2}{1-4(1-\varepsilon_1)(1-\varepsilon_2)E_3^2(\tau_{\nu 0})} \times \left\{\varepsilon_1 i_{b\nu}(T_1) + 2(1-\varepsilon_1)\left[\varepsilon_2 i_{b\nu}(T_2)E_3(\tau_{\nu 0}) + \int_0^{\tau_{\nu 0}} i_{b\nu}(T(\tau_\nu^*))(E_2(\tau_\nu^*) + 2(1-\varepsilon_2)E_3(\tau_{\nu 0}) \times E_2(\tau_{\nu 0}-\tau_\nu^*))\, d\tau_\nu^*\right]\right\},$$

$$i_\nu^-(\tau_{\nu 0}) = \frac{n_\nu^2}{1-4(1-\varepsilon_1)(1-\varepsilon_2)E_3^2(\tau_{\nu 0})} \times \left\{\varepsilon_2 i_{b\nu}(T_2) + 2(1-\varepsilon_2)\left[\varepsilon_1 i_{b\nu}(T_1)E_3(\tau_{\nu 0}) + \int_0^{\tau_{\nu 0}} i_{b\nu}(T(\tau_\nu^*))(E_2(\tau_{\nu 0}-\tau_\nu^*) + 2(1-\varepsilon_1)E_3(\tau_{\nu 0})E_2(\tau_\nu^*))\, d\tau_\nu^*\right]\right\}, \tag{5}$$

with the exponential integrals $E_n(\xi)$ [15] defined by:

$$E_n(\xi) = \int_0^1 \mu^{n-2}e^{-\xi/\mu}\, d\mu.$$

The spectral radiative flux $q_{rad,\nu}$ and its divergence at location $\tau_\nu = E_\nu x$ can be expressed by

$$q_{rad,\nu}(\tau_\nu) = 2\pi\left\{i_\nu^+(0)E_3(\tau_\nu) + \int_0^{\tau_\nu} n_\nu^2 i_{b\nu}(T(\tau_\nu^*))E_2(\tau_\nu-\tau_\nu^*)\, d\tau_\nu^* - i_\nu^-(\tau_{\nu 0})E_3(\tau_{\nu 0}-\tau_\nu) - \int_{\tau_\nu}^{\tau_{\nu 0}} n_\nu^2 i_{b\nu}(T(\tau_\nu^*)) \times E_2(\tau_\nu^*-\tau_\nu)\, d\tau_\nu^*\right\}, \tag{6}$$

$$\frac{d}{dx}q_{rad,\nu}(\tau_\nu) = E_\nu 2\pi\left\{2n_\nu^2 i_{b\nu}(T(\tau_\nu)) - i_\nu^+(0)E_2(\tau_\nu) - \int_0^{\tau_\nu} n_\nu^2 i_{b\nu}(T(\tau_\nu^*)) \times E_1(\tau_\nu-\tau_\nu^*)\, d\tau_\nu^* - i_\nu^-(\tau_{\nu 0})E_2(\tau_{\nu 0}-\tau_\nu) - \int_{\tau_\nu}^{\tau_{\nu 0}} n_\nu^2 i_{b\nu}(T(\tau_\nu^*))E_1(\tau_\nu^*-\tau_\nu)\, d\tau_\nu^*\right\}. \tag{7}$$

Equation (1) together with equations (7) and (5) defies an analytical solution. Thus the temperature profile and the radiative intensities have to be calculated numerically in an iterative procedure for given temperatures and emissivities at the boundaries.

2.2. *Numerical solution*

The numerical solution developed in this work combines approaches and ideas from several works reported previously ([14, 16–18] and especially [12]). Methods for integrating equation (3) with respect to wavelength, spatial coordinate and time are the following.

Wavelength. To describe the strong wavelength dependence of radiative properties E_ν and n_ν a band model, in practice with 40 bands, has been used. Defining M bands (index k), equations (4)–(7) may be adapted to each band by substitution of ν by an index k. The divergence of radiative flux q_{rad} can then be expressed as

$$\frac{\mathrm{d}}{\mathrm{d}x} q_{\mathrm{rad}} = \sum_{k=1}^{M} \frac{\mathrm{d}}{\mathrm{d}x} q_{\mathrm{rad},k}. \tag{8}$$

Spatial (optical) coordinate. The medium is divided into N sublayers of variable thickness (in practice up to 80). The spatial coordinates $0, x_1, \ldots, x_i, \ldots, x_N = d$ correspond to the optical coordinates $0, \tau_{\nu,1}, \ldots, \tau_{\nu,i}, \ldots, \tau_{\nu,N} = \tau_{\nu 0}$. They define the boundaries between these sublayers. For a fixed x position the optical coordinate τ_ν is varying with ν due to the spectral dependence of E_ν. In order to calculate integrals such as

$$\int_0^{\tau_{\nu 0}} n_\nu^2 i_{\mathrm{b}\nu}(T(\tau_\nu^*)) \cdot f(\tau_\nu, \tau_\nu^*)\, \mathrm{d}\tau_\nu^* \tag{9}$$

in equations (6) and (7), the intensity of the blackbody radiation $i_{\mathrm{b}\nu}(T(\tau_\nu))$ is interpolated linearly in each sublayer. In the two sublayers adjacent to the point of the grid, where temperature and heat flux are calculated, a second-order polynomial approximation is used, as proposed by Schwander [12]. Especially for an optically thick medium this gives the correct result as expected from the Rosseland diffusion approximation [14]. As the functions $f(\tau_\nu, \tau_\nu^*)$ consist of some constants and the exponential integrals $E_n(\tau_\nu^*)$, which are easily integrated and differentiated, integrals (9) may be calculated sublayer by sublayer by partial integration (see the Appendix).

Time. Though in this work only steady state heat flux is treated, we started to solve the non-stationary problem. The change of temperature with time in equation (1) is calculated using the combined implicit/explicit finite difference Crank–Nicholson method (CNM) [19].

As the CNM and the description of integrals (9) allow one to use a variable grid width for spatial coordinates, it is possible to concentrate the grid points at the physically important regions near the boundaries, where interaction of radiation and conduction is most important. In order to get the best results for a certain number of sublayers, for any value of optical thickness we choose a hyperbolic density variation for the grid points; starting at a relative distance to boundary $x/d = 10^{-4}$ (for special investigations 10^{-5}) sublayers become broader towards the middle of the system. In order to correctly describe the temperature gap in the hypothetical case of pure radiation additionally a grid point at $x/d = 10^{-10}$ was selected at each boundary.

The original CNM for diffusion problems couples every grid point only with the neighbouring ones. In order to include the long range radiation field the interaction of all grid points with each other (see Appendix) has to be included. Instead of a linear system, described by a matrix equation with tridiagonal matrix in the original CNM, now a matrix equation with a completely filled matrix has to be solved.

The approximation for the development

$$T_{n+1}^4 - T_n^4|_{x_i} \approx 4T_n^3 \cdot (T_{n+1} - T_n)|_{x_i} \tag{10}$$

between times t_n and t_{n+1} linearizes the system. It is, however, without any influence on the steady state result.

The CNM is unconditionally stable. However, for large time steps it tends to oscillate. Temperature values at each grid point—we use for the steady state solution infinitely large time steps ($1/\Delta t = 0$)—oscillate between two extrema. Using the arithmetic mean of the current temperature and the one calculated for the next 'time' step gives an iterative method, which is also unconditionally stable, but which converges fast into the steady state result. For grey media the strong criterion used to stop iterations, i.e. a temperature change at every grid point smaller than 10^{-17}, is already reached with five iterations, for non-grey media with less than 20 iterations. The relative variation of the calculated heat flux within the layer, which in the stationary state should be constant, ranges from 10^{-3} for the worst case of a strong non-grey radiation-dominated system, with strong interaction of radiation and conduction near the boundaries, down to 10^{-9} for grey media without conduction.

The described numerical method is stable for any ratio of radiative to conductive heat transfer and any emissivity at the boundaries.

2.3. *Comparison with published data*

The theoretical work of Heaslet and Warming [20] considers the radiative heat transfer and temperature profiles in a planar, non-scattering medium between opaque grey diffusive boundaries, but without conduction. The principal aim of their work has been to provide a standard of accuracy. As the reported results are based on the first moments ($\alpha_0, \beta_0, \alpha_1, \beta_1$) of the X- and Y-functions of Chandrasekhar [22] (Ambartsumians functions), calculated numerically by Sobouti in 1962 [21], accuracy is limited to the accuracy of the tabulated values (four decimals, $\alpha_0 + \beta_0$ should be exactly 2, but is 1.9999). This explains the deviations

Table 1. Comparison of temperature gaps and heat fluxes for grey media between black walls ($\varepsilon = 1$), expressed by the dimensionless numbers α_0, β_0 and Q. The values on the left side for $\tau_0 \geqslant 10$ have been calculated by the formula given by Heaslet [20]

$\varepsilon = 1$	Heaslet [20, 21]			This study		
τ_0	α_0	β_0	Q	α_0	β_0	Q
0.1	1.1419	0.8579	0.9157	1.14202	0.85798	0.91570
0.2	1.2228	0.7771	0.8491	1.22287	0.77713	0.84918
0.3	1.2838	0.7161	0.7934	1.28385	0.71615	0.79358
0.4	1.3331	0.6668	0.7458	1.33320	0.66680	0.74586
0.5	1.3746	0.6253	0.7040	1.37467	0.62533	0.70417
0.6	1.4103	0.5896	0.6672	1.41034	0.58966	0.66731
0.8	1.4692	0.5307	0.6046	1.46921	0.53079	0.60475
1.0	1.5163	0.4836	0.5532	1.51630	0.48370	0.55341
1.5	1.6024	0.3975	0.4572	1.60240	0.39760	0.45733
2.0	1.6615	0.3384	0.3900	1.66150	0.33840	0.39007
2.5	1.7051	0.2948	0.3401	1.70516	0.29484	0.34018
3.0	1.7386	0.2613	0.3016	1.73868	0.26132	0.30166
10	1.8989	0.1011	0.1167	1.89892	0.10108	0.11675
100	1.9886	0.0114	$1.3147 \cdot 10^{-2}$	1.98862	0.01138	$1.3147 \cdot 10^{-2}$
1000	1.9988	0.0012	$1.3314 \cdot 10^{-3}$	1.99886	0.00114	$1.3315 \cdot 10^{-3}$
10 000	1.9999	0.0001	$1.3331 \cdot 10^{-4}$	1.99990	0.00010	$1.3331 \cdot 10^{-4}$

α_0 and β_0 determine the temperature gaps $T_1 - T(0)$ and $T(d) - T_2$, Q is the dimension less heat flux. For $\varepsilon = 1$ the following relations are valid:

$$2 \cdot \frac{T^4(x=0) - T_2^4}{T_1^4 - T_2^4} = \alpha_o; \quad 2 \cdot \frac{T^4(x=d) - T_2^4}{T_1^4 - T_2^4} = \beta_0; \quad Q = \frac{q}{\sigma T_1^4 - \sigma T_2^4}.$$

Table 2. Comparison for grey media between diffusely reflecting boundaries with $\varepsilon = 0.05$

$\varepsilon = 0.05$	Heaslet [20, 21]		This study	
τ_0	$\frac{T_1^4 - T^4(0)}{T_1^4 - T_2^4}$	Q	$\frac{T_1^4 - T^4(0)}{T_1^4 - T_2^4}$	Q
0.1	0.4979	$2.5581 \cdot 10^{-2}$	0.49802	$2.5581 \cdot 10^{-2}$
0.2	0.4966	$2.5525 \cdot 10^{-2}$	0.49665	$2.5525 \cdot 10^{-2}$
0.3	0.4955	$2.5471 \cdot 10^{-2}$	0.49544	$2.5471 \cdot 10^{-2}$
0.4	0.4943	$2.5419 \cdot 10^{-2}$	0.49432	$2.5419 \cdot 10^{-2}$
0.5	0.4933	$2.5368 \cdot 10^{-2}$	0.49325	$2.5368 \cdot 10^{-2}$
0.6	0.4922	$2.5317 \cdot 10^{-2}$	0.49222	$2.5317 \cdot 10^{-2}$
0.8	0.4902	$2.5218 \cdot 10^{-2}$	0.49022	$2.5219 \cdot 10^{-2}$
1.0	0.4883	$2.5121 \cdot 10^{-2}$	0.48828	$2.5122 \cdot 10^{-2}$
1.5	0.4836	$2.4884 \cdot 10^{-2}$	0.48361	$2.4885 \cdot 10^{-2}$
2.0	0.4791	$2.4652 \cdot 10^{-2}$	0.47909	$2.4654 \cdot 10^{-2}$
2.5	0.4747	$2.4426 \cdot 10^{-2}$	2.47468	$2.4428 \cdot 10^{-2}$
3.0	0.4703	$2.4204 \cdot 10^{-2}$	0.47036	$2.4207 \cdot 10^{-2}$
10	0.4173	$2.1475 \cdot 10^{-2}$	0.41731	$2.1480 \cdot 10^{-2}$
100	0.1704	$8.7669 \cdot 10^{-3}$	0.17030	$8.7685 \cdot 10^{-3}$
1000	0.0246	$1.2673 \cdot 10^{-3}$	0.02445	$1.2678 \cdot 10^{-3}$
10 000	0.0026	$1.3264 \cdot 10^{-4}$	0.00233	$1.3271 \cdot 10^{-4}$

For equal emissivities at both boundaries ($\varepsilon_1 = \varepsilon_2$) there is

$$\frac{T_1^4 - T^4(0)}{T_1^4 - T_2^4} = \frac{T^4(d) - T_2^4}{T_1^4 - T_2^4}.$$

of the results of this study to that of Heaslet for optical thicknesses $\tau_0 < 10$ as depicted in Tables 1 and 2.

Further comparison has been done with data for combined radiative and conductive heat transfer in grey media published by Viskanta and Grosh [6, 7], non-grey media (2 band model) with black walls published by Crosbie [8] and Doornink [10] and grey media published by Anderson [9]. Most reliable seem the data of Crosbie that have been reproduced in this study with relative deviations smaller then 10^{-4}. For the other data the deviations are in maximum 1% (Doornink) and 0.5% (Anderson).

Table 3 shows the high precision with which the temperature profile may also be calculated, especially

Table 3. Comparison of several numerical solutions for a temperature profile. Data from Heaslet are based on α_0 and β_0 as tabulated by Sobouti; the values in the brackets reflect their uncertainty

x/d	Heaslet [20]	Saulnier [23] (103 nodes)	Schwander [12] (101 points)	This study (80 points)
0.0	382.821 (382.833)	382.85	381.80	382.833
0.1		396.49	396.50	396.498
0.2		407.32	407.30	407.325
0.3		416.78	416.76	416.791
0.4		425.41	425.39	425.416
0.5	433.455 (exact)	433.45	433.43	433.454
0.6		441.06	441.05	441.069
0.7		448.39	448.38	448.392
0.8		455.56	455.54	455.565
0.9		462.82	462.79	462.825
1.0	471.311 (471.317)	471.21	471.29	471.311

Grey medium, no conduction, $\tau_0 = 1$, $\varepsilon = 1$, $T_1 = 500$ K, $T_2 = 300$ K.

near the boundaries. The data of Heaslet are standard again using the tabulated values of Sobouti. The values in the brackets reflect the uncertainty in α_0 and β_0.

3. EXPERIMENTAL INVESTIGATIONS

The heat fluxes of three monolithic SiO_2-aerogels with densities of 5, 50 and 220 kg m^{-3} and thicknesses of 17.5, 6.7 and 7.9 mm, respectively, have been investigated. The first sample with a density of only four times that of dry air has the appearance of frozen fog, the last one with a density of a tenth of that of bulk glass has the character of a light solid body. To avoid the influence of adsorbed water on the IR-optical and heat transfer measurements the samples were heated to about 600 K in vacuum for several hours prior to the experiments.

3.1. *Infrared optical measurements*

The spectral specific extinction e as depicted in Fig. 2 was derived from transmission measurements performed with a Fourier-transform-infrared (FTIR)-spectrometer. Clearly visible is the drastic variation of e with wavelength, exceeding four orders of magnitude. The region between 5 and 30 μm is characterized by large absorption bands of vibrational excitations of the Si-O network at 9.5, 12.5 and 21 μm. There is no significant difference between the various aerogels and no difference to data of bulk material [24]. For long wavelengths ($\Lambda > 30$ μm), however, the structure of the individual aerogel material influences the absorption. For short wavelength ($\Lambda < 5$ μm) 'impurities', organic components and remaining OH-groups determine the absorption. Variations are caused by different preparation and different pre-treatment with temperature in oxidizing atmosphere or in vacuum.

3.2. *Heat transfer measurements*

The experimental heat transfer data were derived with an evacuable, externally load-controlled guarded hot plate system (see Fig. 3). The diameter of the specimens is 20 cm. The metering section is 12 cm ∅. A temperature controlled cylindrical guard allows one to cover a large temperature range ($T = 100$–1000 K). From two measurements at the same mean temperature, but with different temperature differences across the specimens (between 2 and 20 K), radial heat losses and errors in measured temperatures could be corrected [5, 25]. In the following figures the amount of corrections to the measured data are depicted as 'error bars'. The overall uncertainty is estimated to be less than 5%.

Four series of thermal measurements were performed on each sample: emissivities $\varepsilon = 0.04$ and $\varepsilon = 0.7$, with gas (N_2) and evacuated. The covered temperature range was 100–650 K. At 300 K additionally the internal gas pressure was varied from 10^{-4} hPa to 1000 hPa.

4. COMPARISON OF EXPERIMENTAL AND NUMERICAL DATA

For the numerical calculations of the heat fluxes of the aerogel samples some additional information is needed.

Spectral data

A flexible, temperature and sample dependent subdivision of the IR-spectra to 40 bands has been used. Neglecting any coupling between radiation and conduction and between spectral bands, the radiative flux in each band was chosen to be about the same using

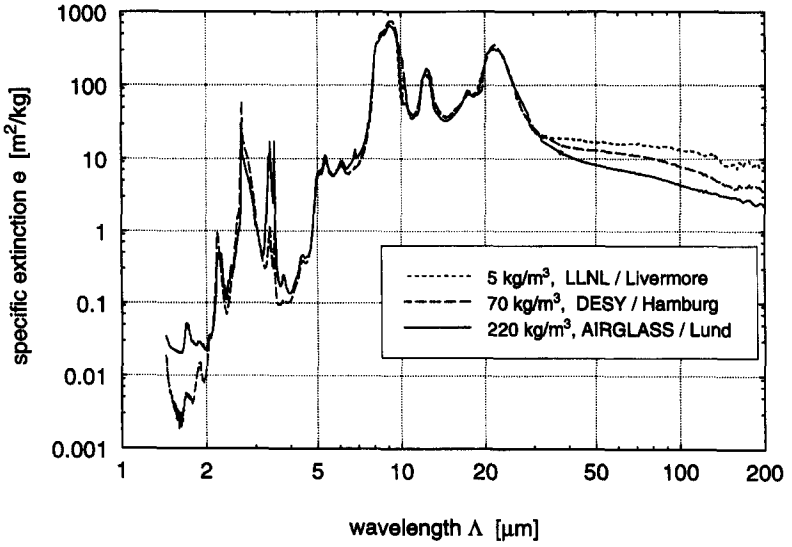

Fig. 2. Specific extinction coefficient e vs wavelength for aerogels with different densities and of different origin.

$$q_{\text{rad,band}} \propto \frac{f^*_{\Lambda_1 T} - f^*_{\Lambda_2 T}}{\frac{3}{4} e_{\Lambda_1 - \Lambda_2} \rho d + 1}, \tag{11}$$

with the limits of the band Λ_1, Λ_2 and the fractional function of the 2nd kind $f^*_{\Lambda T}$ (see ref. [16]). For example see Fig. 4. The influence of the index of refraction n_r is small (about 10% for the most dense sample). As an approximation, data calculated with the Clausius–Mossotti formula from the data of quartz glass [24] have been used.

Solid conductivity λ_{sc}

In the investigated temperature range for SiO_2-aerogels the same temperature dependence is expected as for vitreous silica [3]; data have been taken from refs. [11] and [26]. A geometrical factor that describes the porous medium may be evaluated from measured heat transfer coefficients at low temperatures.

Gaesous conductivity λ_{gas}

In this porous system gaseous contribution may be described by Knudsen's formula [27]

$$\lambda_{\text{gas}}(T) = \frac{\lambda_{\text{gas},0}(T)}{1 + 2\beta \frac{l_{\text{gas}}(T)}{D}}. \tag{12}$$

Temperature dependent values for the conductivity of the free nitrogen gas $\lambda_{\text{gas},0}(T)$ and the mean free path of the gas molecules $l_{\text{gas}}(T)$ have been taken from literature [28]. β is a constant assumed to be 3. The characteristic pore size D may be evaluated for each sample from the measured dependence of the heat transfer coefficient with gas pressure. For example see Fig. 5. The fits due to the Knudsen formula (solid lines) give the same pore size for both surface emissivities: $D = 180$ nm.

In Figs. 6–8 measured and calculated transfer coefficients k are plotted vs the third power of mean temperature T^3_{rad}, the parameter is the surface emissivity ε; data for evacuated and non-evacuated specimens are shown. In such plots a linear variation is expected for grey media with temperature independent contributions of conduction and no interaction with radiation.

For all measurements experimental and numerical results coincide within the experimental uncertainties. The systematic deviations of the data for the evacuated samples with low ε surfaces are due to difficulties in machining the samples plane parallel. The surface roughness of several tenth of millimeters becomes important when the interaction of radiation with conduction close to the boundaries has a large influence on total heat transfer. The presence of larger 'pores' can also clearly be seen when the gas pressure is varied [5]. The additional heat resistance at the surface in the evacuated sample, due to an insufficient contact, is removed in the non-evacuated case, where experimental and numerical values coincide again.

In Figs. 6 and 7 additionally, the contributions of solid conduction are depicted. At 300 K the solid conduction is the dominant transfer mechanisms for the 220 kg m^{-3} sample. for the 50 kg m^{-3} sample, its contribution is about one third of the total heat transfer, for the 5 kg m^{-3} sample no solid contribution can be deduced from the measurement any more.

If the conductivity λ_{cond} is enlarged by increasing the gas pressure, within the 220 kg m^{-3} sample no additional interaction of radiation with conduction in comparison to the evacuated sample is seen; the difference of the coefficient k between the non-evacuated and the evacuated sample is the same for both emissivities; the gaseous contribution is simply added. Quite different is the situation for the 5 kg m^{-3} sample. For the evacuated sample the radiative heat exchange

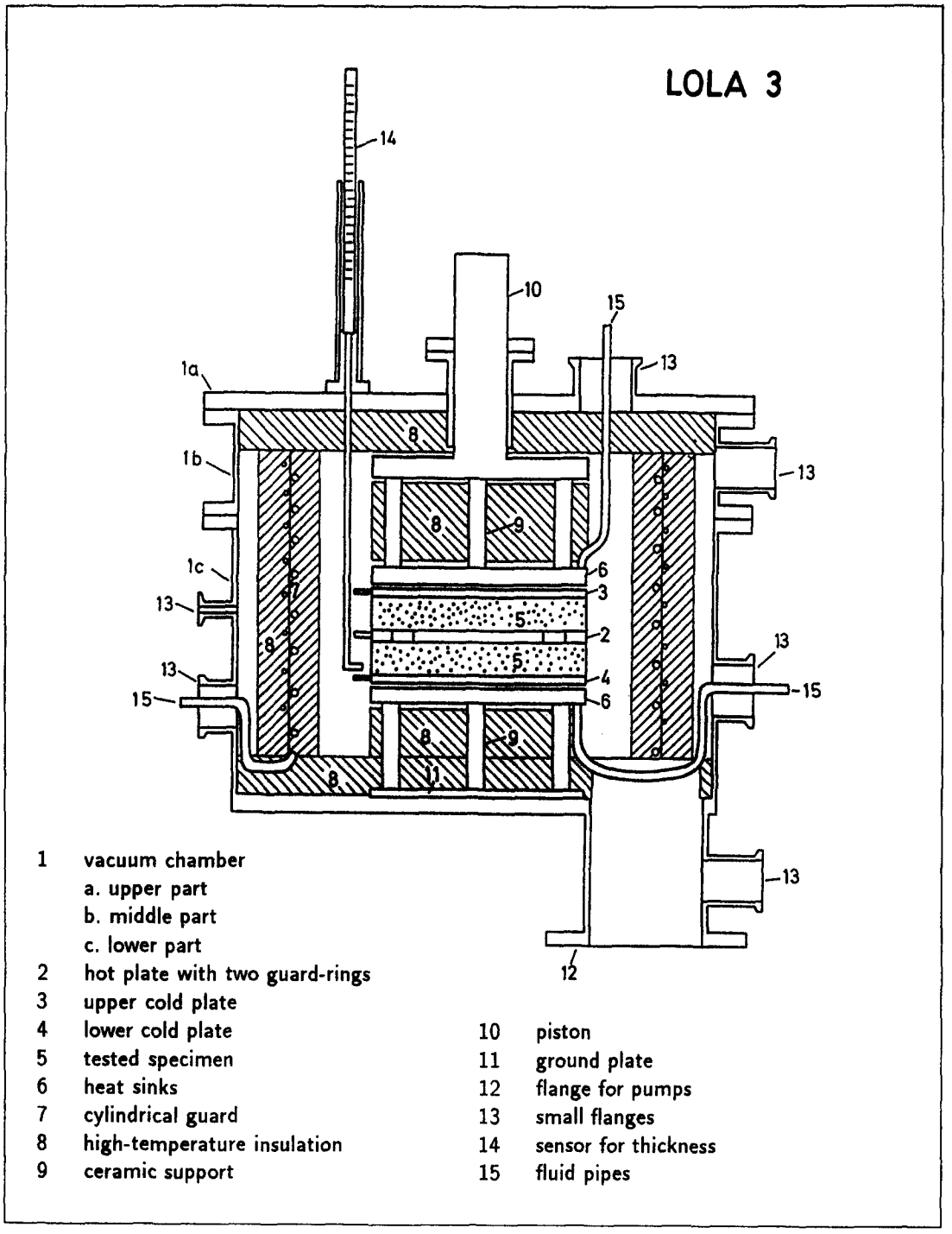

Fig. 3. Guarded hot plate apparatus LOLA III, which can be evacuated and externally pressure loaded.

is about the same as that between two surfaces facing each other and having an emissivity $\varepsilon = 0.04$ ($k = 4\sigma T_{\text{rad}}^3/(2/\varepsilon - 1)$, see interrupted dashed lines in Fig. 8). There is just a weak attenuation of the radiative flux due to the presence of the specimen. For nearly black boundaries ($\varepsilon = 0.74$) the radiative exchange between the two surfaces is reduced by about 50%, corresponding to an effective optical thickness of about 1. Conduction via the solid skeleton is extremely small for the 5 kg m^{-3} sample. Due to the interaction of conduction and radiation, otherwise larger heat losses would be expected for the low emissivity boundaries $\varepsilon = 0.04$ (see below). In the lower plot of Fig. 8 the dashed line represents the heat transfer one would expect for a simple additive contribution of gaseous conduction. In reality the interaction of the two trans-

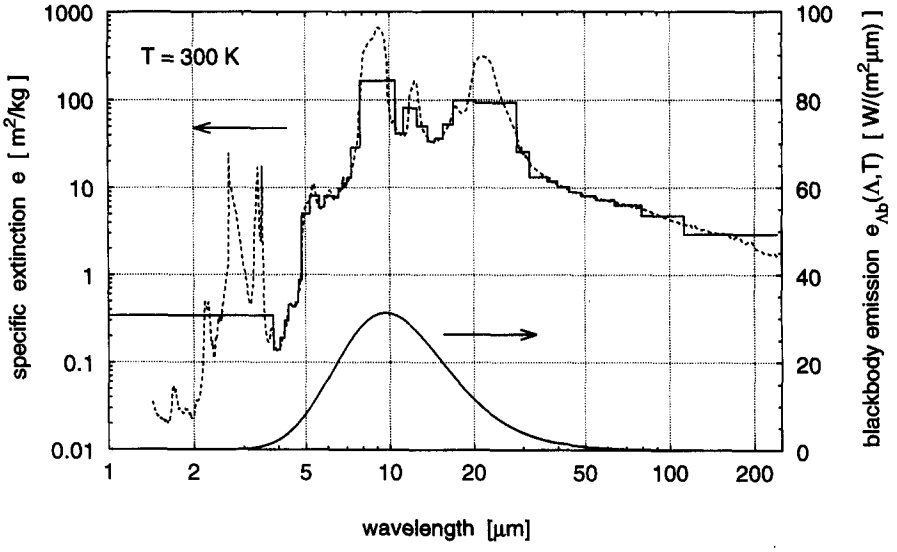

Fig. 4. Subdivision of the extinction spectrum into 40 bands for the sample with density $\rho = 220$ kg m^{-3} at 300 K and the spectral emissive power of a blackbody at 300 K.

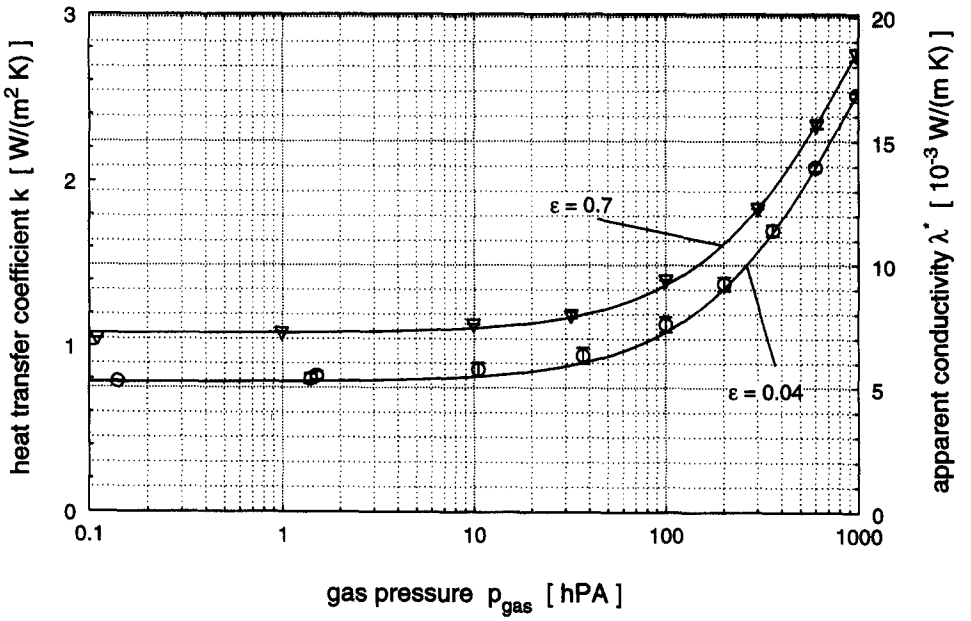

Fig. 5. Heat transfer coefficient and apparent thermal conductivity vs internal gas pressure for the sample with density $\rho = 50$ kg m^{-3}, thickness $d = 6.7$ mm, measured at $T = 293$ K.

fer mechanisms results in a combined heat transfer that is much larger than the additive contributions—more than twice for temperatures above 370 K.

This effect was studied in more detail by varying the gas pressure (Fig. 9). The preparation of this extremely light aerogel sample has been very difficult. The investigated aerogel sample had a rough surface and additionally it had several large cracks. For the measurement with nearly black walls ($\varepsilon = 0.74$), where the effect of interaction is expected to be very small, a fit according to the Knudsen formula with two distinguished 'pore sizes' and different volume fractions fits the measured data quite well. The derived volume fractions and pore sizes (90% 2 μm pores and 10% 1.8 mm 'pores') are plausible. Using this result as input for the numerical calculations of the low ε system the theoretical values reflect the shape of the measured dependence of k on gas pressure. They are somewhat larger than the measured data as the thermal contact of the sample with the boundaries is not perfect. The solid line shows the thermal transfer coefficient of the combined heat transfer as the function of the gas pressure for a single pore size (2 μm). This may be compared to the simple model of additive

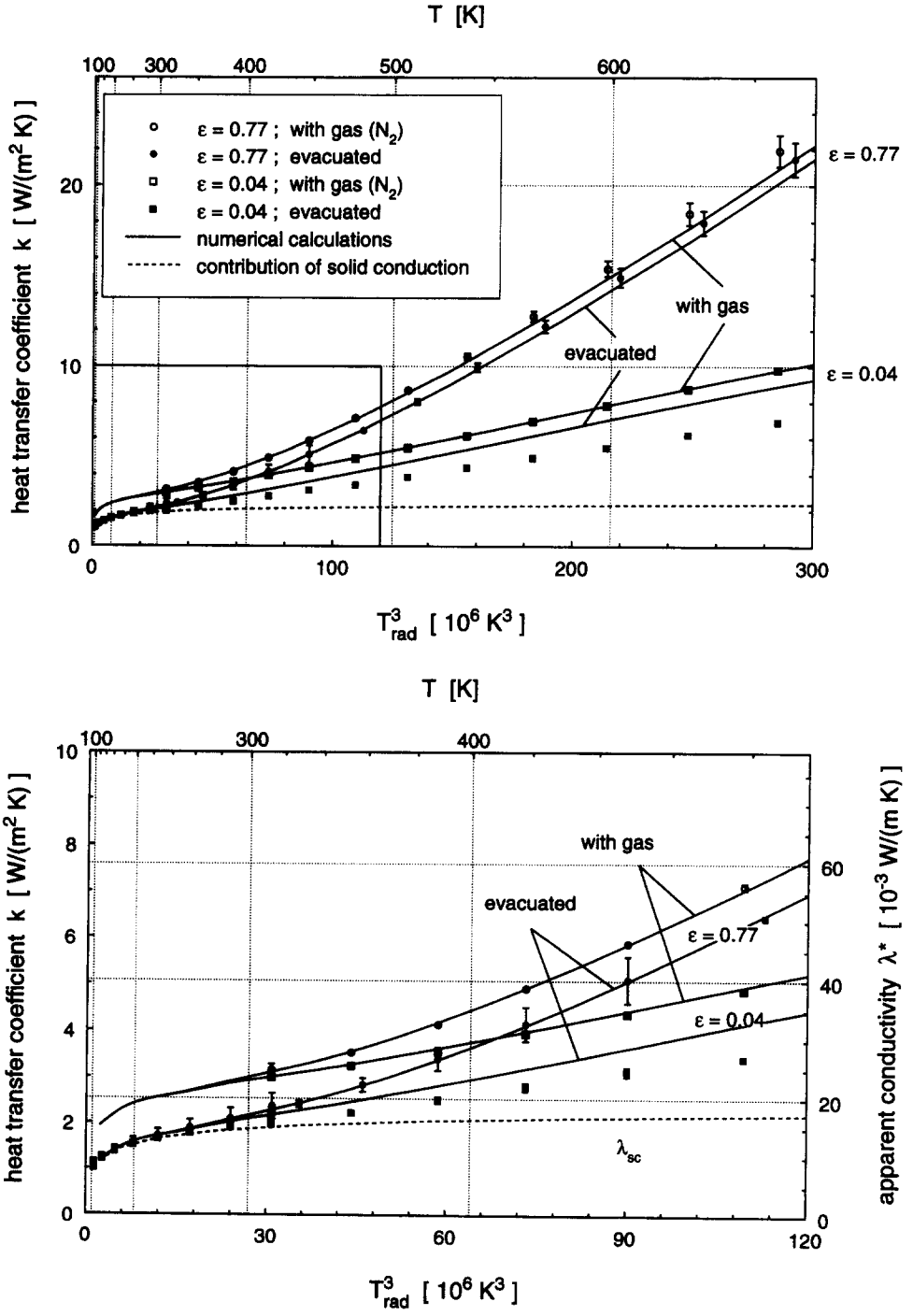

Fig. 6. Measured and calculated heat transfer coefficient k vs T^3_{rad} for an aerogel tile with $\rho = 220$ kg m^{-3}, thickness $d = 7.9$ mm.

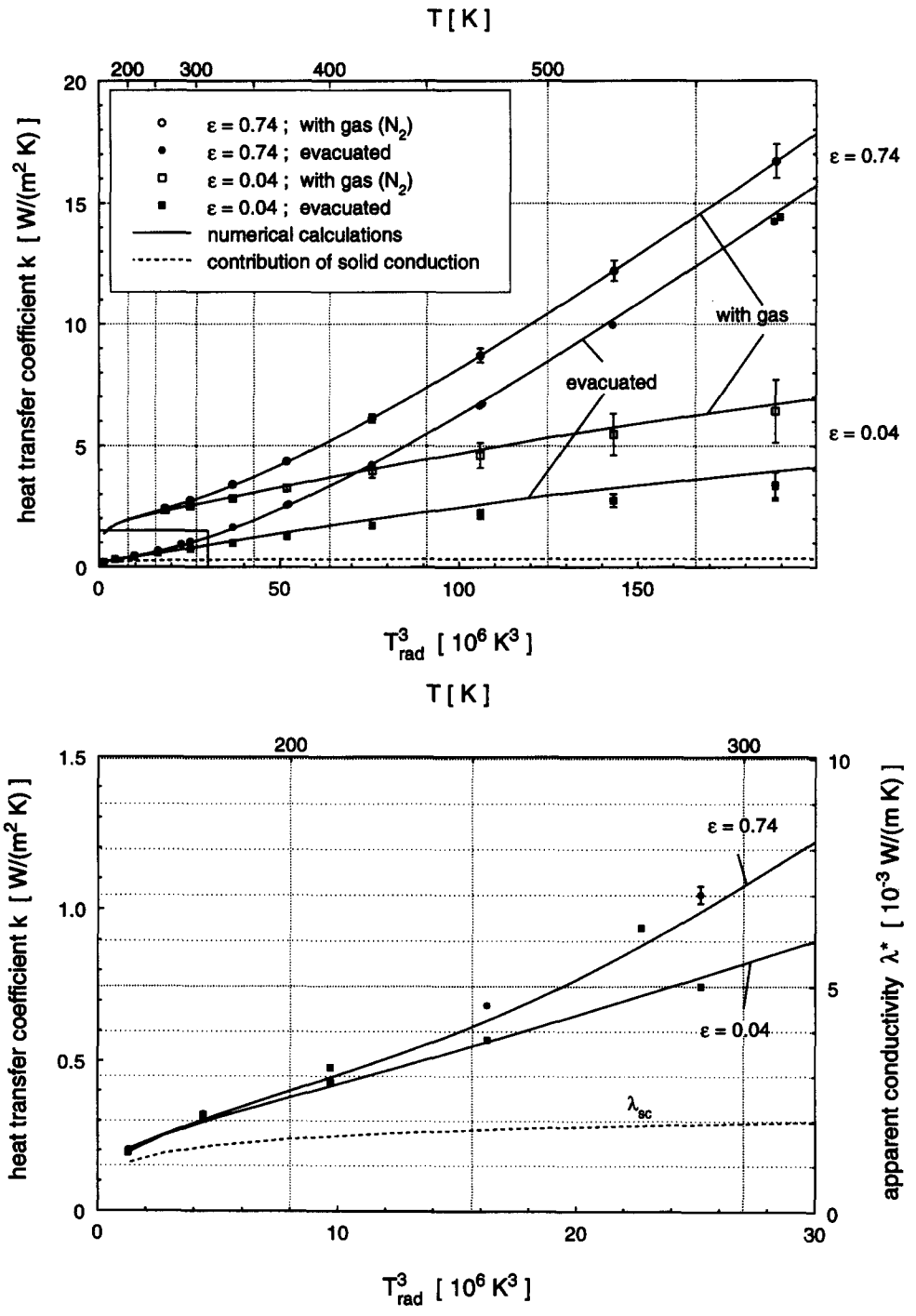

Fig. 7. Measured and calculated heat transfer coefficient k vs T^3_{rad} for an aerogel tile with $\rho = 50$ kg m^{-3}, thickness $d = 6.7$ mm.

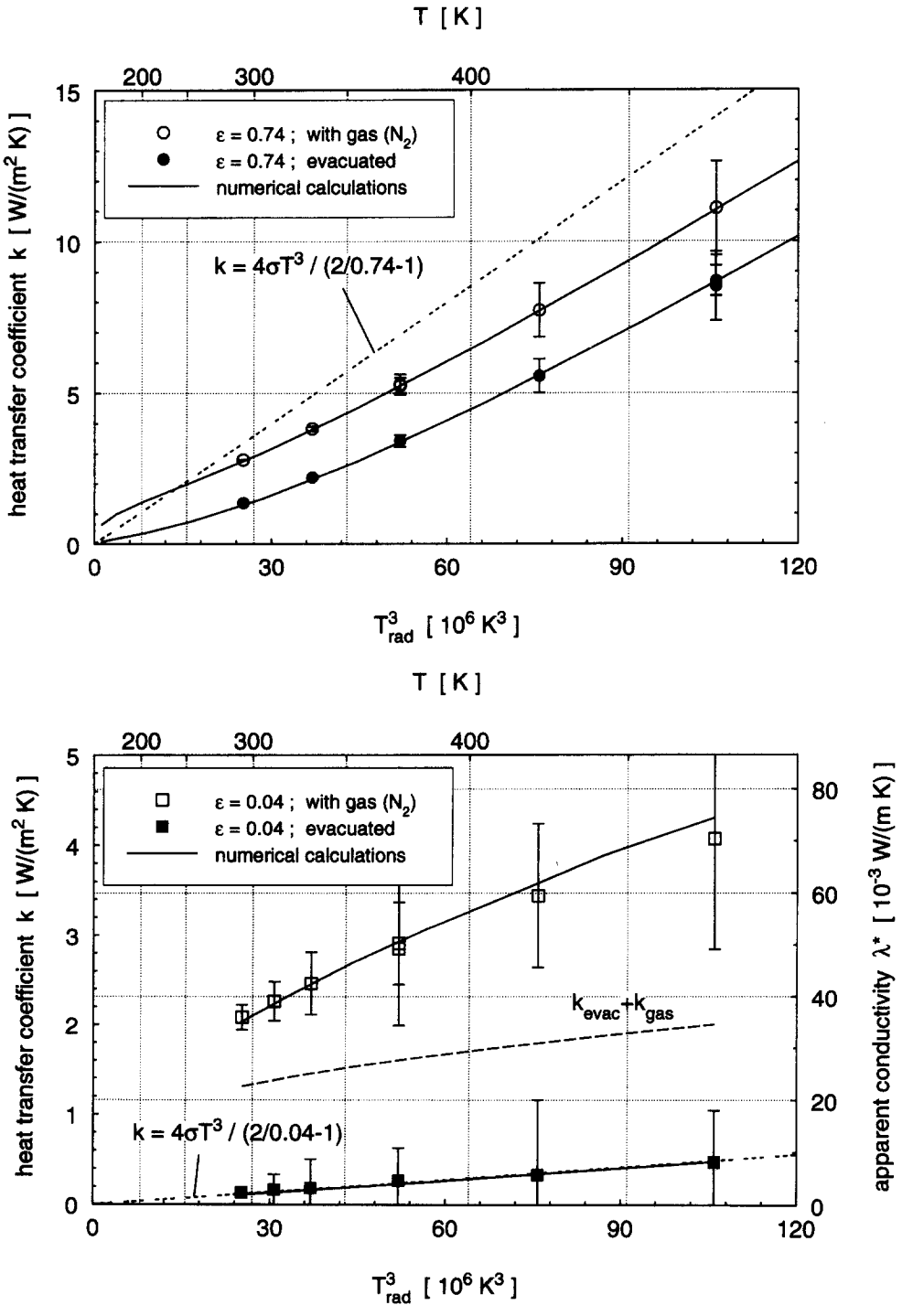

Fig. 8. Measured and calculated heat transfer coefficient k vs T^3_{rad} for an aerogel tile with $\rho = 5$ kg m^{-3}, thickness $d = 17.5$ mm.

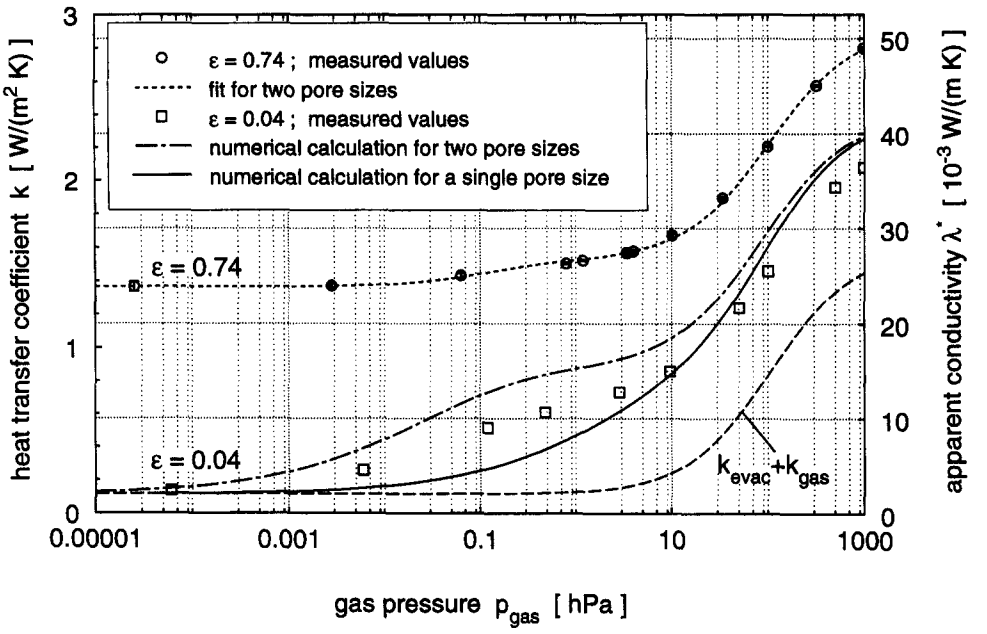

Fig. 9. Measured and calculated heat transfer coefficient k vs internal gas pressure for an aerogel sample with $\rho = 5$ kg m^{-3}, thickness $d = 17.5$ mm at temperature $T = 293$ K.

components, $k_{evac}+k_{gas}$ (lower dashed line in Fig. 9). Due to the interaction of radiation with conduction, there is an extraordinarily large influence of even very small gaseous conductivities: for example at 0.1 hPa an additional gaseous conductivity in the porous system of $0.025 \cdot 10^{-3}$ W (m · K)$^{-1}$ enhances the apparent conductivity λ^* from 2.0 to $4.5 \cdot 10^{-3}$ W (m · K)$^{-1}$; the change in apparent conductivity is thus a hundred times larger than the additional gaseous conductivity.

For small temperature differences solid and gaseous conductivity can be assumed to be temperature independent. Under this assumption the mean heat transfer by conduction $\overline{q_{cond}}$ does not depend on the temperature profile inside the medium

$$\overline{q_{cond}} = \frac{1}{d}\int_0^d q_{cond}(x)\,dx$$

$$= -\frac{1}{d}\int_0^d \lambda_{cond}\frac{dT}{dx}dx = -\lambda_{cond}\frac{\Delta T}{d}.$$

Therefore the effect of interaction can be attributed to an increase of the radiative component. This radiative component, which is the total combined heat transfer minus the conductive contribution, as a function of conductivity λ_{cond}, is depicted in Fig. 10. The amount exceeding the horizontal dash–dotted line (no conduction) is due to the interaction. The effect of interaction, which can be noticed as an increase of the radiative component, already starts at extremely small conductive contributions represented by the dotted curve. The interaction contribution increases with increasing λ_{cond} and approaches a constant value when conduction becomes the dominant transfer mechanism (point 6 in Fig. 10) and a linear temperature profile is reached (Fig. 11). Temperature profiles corresponding to the numerated dots 1–6 of Fig. 10 are depicted in Fig. 11. The large amount of radiative heat transfer, despite the low emissivity boundaries, may be attributed to the emission and absorption of radiation in a small aerogel layer near the surfaces. Due to the steep temperature gradient at the boundaries, even for small conductivities, a large amount of heat is transferred from the low emissivity boundary to the adjacent aerogel layer on the hot side. On the cold side correspondingly, heat is transferred from the aerogel layer to the boundary. From these absorbing and emitting 'boundary' layers then radiation is exchanged with the deeper layers of the medium.

5. CONCLUSION

A wide range of optical thickness and ratio of radiative to conductive heat transfer for non-grey media has been studied. Silica aerogels proved to be an ideal medium for studying the interaction of radiation with conduction theoretically, as well as experimentally. For all measurements that cover a wide variation of aerogel density, temperature, internal gas pressure and emissivity of bounding surfaces, experimental and numerical results coincide within the experimental uncertainties.

The developed numerical method is stable for any ratio of radiative to conductive heat transfer and any emissivity of the boundaries. Also the situation in non-grey media, with a very strong dependence of infrared optical properties with wavelength, is described accurately. Its high precision in temperature profile and heat flux allows one to consider even extreme constellations for parameter studies.

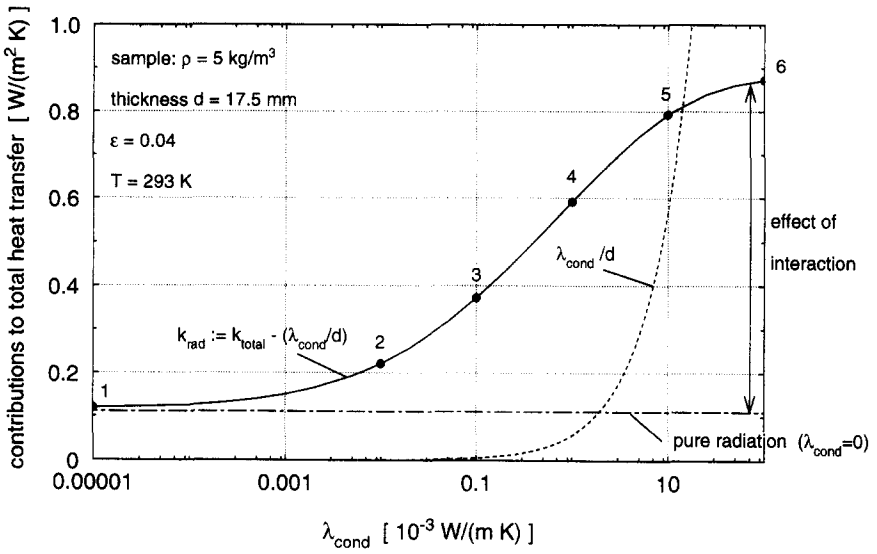

Fig. 10. Contribution of radiation to the total heat transfer including the effect of interaction vs conductivity λ_{cond} (solid curve) for low emissivity boundaries, conductive contribution (dotted curve) and hypothetical radiative contribution without interaction (dash–dotted line).

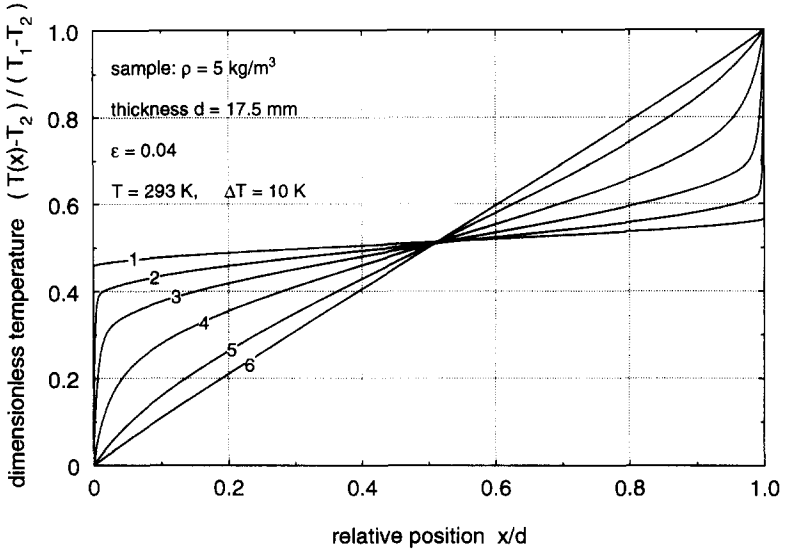

Fig. 11. Temperature in the medium as a function of relative position corresponding to the numerated dots in Fig. 10.

Acknowledgements—This work was supported by the Bavarian Ministry of Economics (Bayerisches Staatsministerium für Wirtschaft, Verkehr und Technologie). We would like to thank Dr L.W. Hrubesh from Lawrence Livermore National Laboratory, Livermore, USA, Dr G. Poelz from DESY, Hamburg, Germany and Dr S. Henning from Airglass AB, Staffanstorp, Sweden for generously providing aerogel specimens.

REFERENCES

1. J. Fricke and A. Emmerling, Aerogels—preparation, properties, applications. In *Chemistry, Spectroscopy and Applications of Sol-Gel Glasses* (Edited by R. Reisfeld and C. K. Jørgensen), pp. 37–87, Structure and Bonding Series. Vol. 77, Springer Heidelberg (1992).
2. J. Fricke, Materials research for the optimization of thermal insulations, *High Temp.-High Press.* **25,** 379–390 (1993).
3. P. Scheuerpflug, M. Hauck and J. Fricke, Thermal properties of silica aerogels between 1.4 and 330 K, *J. Non-Chrystalline Solids* **145,** 196–201 (1992).
4. A. Emmerling and J. Fricke, Scaling properties and structure of aerogels, *J. Sol–Gel Sci.* (in press).
5. U. Heinemann, Wärmetransport in semitransparenten nichtgrauen Medien am Beispiel von SiO_2—Aerogelen, Ph.D. thesis, University of Würzburg (1993).
6. R. Viskanta and R. J. Grosh, Heat transfer by sim-

ultaneous conduction and radiation in an absorbing medium, *Trans. ASME J. Heat Transfer* **C84,** 63–72 (1962).
7. R. Viskanta and R. J. Grosh, Effect of surface emissivity on heat transfer by simultaneous conduction and radiation, *Int. J. Heat Mass Transfer* **5,** 729–734 (1962).
8. A. L. Crosbie and R. Viskanta, Interaction of heat transfer by conduction and radiation in a nongray planar medium, *Wärme Stoffübertragung* **4,** 205–212 (1971).
9. E. E. Anderson and R. Viskanta, Spectral and boundary effects on coupled conduction–radiation heat transfer through semitransparent solids, *Wärme Stoffübertrag* **6,** 14–24 (1973).
10. D. G. Doornink and R. G. Hering, Simultaneous radiative and conductive heat transfer in non-gray media, *J. Quant. Spectrosc. Radiat. Transfer* **13,** 323–332 (1973).
11. T. Kunc, M. Lallemand and J. B. Saulnier, Some new developments on coupled radiative–conductive heat transfer in glasses—experiments and modelling, *Int. J. Heat Mass Transfer* **27,** 2307–2319 (1984).
12. D. Schwander, G. Flamant and G. Olalde, Effects of boundary properties on transient temperature distributions in condensed semi-transparent media, *Int. J. Heat Mass Transfer* **33,** 1685–1695 (1990).
13. A. A. Men, Specular-diffuse reflection of radiation at the limits of a plane layer for combined radiant and conductive heat transfer, *Heat Transfer—Soviet Res.* **4,** 167–173 (1972).
14. R. Siegel and J. R. Howell, *Thermal Radiation Heat Transfer* (2nd Edn), Chap. 14. McGraw-Hill, New York (1981).
15. M. Abramowitz and I. A. Stegun, *Pocketbook of Mathematical Functions*, p. 56. Verlag Harri Deutsch, Thun, Frankfurt/Main (1984).
16. M. N. Özişik, *Radiative Transfer*. Wiley, New York (1973).
17. R. Viskanta and E. E. Anderson, Heat transfer in semitransparent solids. In *Advances in Heat Transfer* (Edited by T. F. Irvine Jr and J. P. Hartnett), Vol. 11, pp. 317–441. Academic Press, New York (1975).
18. R. Viskanta, Radiation heat transfer: interaction with conduction and convection and approximate methods in radiation, *Proceedings of the 7th International Heat Transfer Conference*, pp. 103–121, München (1982).
19. W. H. Press, B. P. Flannery, S. A. Teukolsky and W. T. Vetterling, *Numerical Recipes in Pascal* (1st Edn), Chap. 17. Cambridge University Press, Cambridge (1986).
20. M. A. Heaslet and R. F. Warming, Radiative transport and wall temperature slip in a planar medium, *Int. J. Heat Mass Transfer* **8,** 979–994 (1965).
21. Y. Sobouti, Chandrasekhar's *X*-, *Y*-, and related functions, *Astrophys. J. Suppl. Ser.* **7,** 411–560 (1962).
22. S. Chandrasekhar and D. Elbert, The *X*- and *Y*-functions for isotropic scattering (I) + (II), *J. Astrophys.* **115,** 244–278 (1952).
23. J. B. Saulnier, La modélisation thermique et ses applications aux transferts couplés et au contrôle actif, Ph.D. thesis, Université de Poitiers, Poitiers (1980), cited by [12].
24. V. A. Petrov and S. V. Stepanov, Radiation characteristics of quartz glasses spectral radiation power, *Teplofizika Vysokikh Temperatur* **13,** 335–345 (1975).
25. J. Hetfleisch, Physics Department of the University of Würzburg, private communication.
26. Y. S. Touloukian, R. W. Powell, C. Y. Ho and P. G. Klemens, *Thermal Conductivity—Nonmetallic Solids* (1st Edn), Vol. 2 of Thermophysical Properties of Matter Data Series, p. 193. Plenum Press, New York (1970).
27. M. Knudsen, Die molekulare Wärmeleitung der Gase und der Akkommodationskoeffizient, *Annalen der Phys. IV. Folge* **34,** 593–656 (1911).
28. R. C. Weast, M. J. Astle and W. H. Beyer (Editors), *Handbook of Chemistry and Physics* (64th Edn), p. F3. CRC Press, Boca Raton, FL (1984).

APPENDIX

DEVELOPMENT OF EQUATIONS

For easier reading the index k of the optical coordinate $\tau_{k,i} = E_k \cdot x_i$ has been omitted. The fraction of blackbody emission in band k, designed by $i_k(T)$, is calculated by

$$i_k(T) = \int_{\nu_2}^{\nu_1} i_{b\nu}\,\mathrm{d}\nu = (f_{0-\Lambda T}(\Lambda_1 \cdot T) - f_{0-\Lambda T}(\Lambda_2 \cdot T))\frac{\sigma T^4}{\pi}, \tag{A1}$$

Λ_1 and Λ_2 are the wavelengths at the band limits in vacuum: $\Lambda_1 = c_0/\nu_1$ and $\Lambda_2 = c_0/\nu_2$. The 'fractional function of the 1st kind' $f_{0-\Lambda T}$ (see ref. [16]) describes the fraction of blackbody emission, emitted in wavelength interval $[0, \Lambda]$. It is a function of $\Lambda \cdot T$. Values may be calculated by polynomial and series expansions (see the Appendix in ref. [14]).

Divergence of radiative heat flux in band k [*see equation* (7)]

$$\begin{aligned}\frac{\mathrm{d}}{\mathrm{d}x} q_{\mathrm{rad},k}(x_i) = &-2\pi E_k \{n_k^2 (F_1(\tau_i) + F_2(\tau_i)) \\ &+ (i_k^+(0) - n_k^2 i_k(0)) \cdot E_2(\tau_i) \\ &+ (i_k^-(\tau_0) - n_k^2 i_k(\tau_0)) \cdot E_2(\tau_0 - \tau_i)\}, \end{aligned} \tag{A2}$$

with the terms from the linear interpolation of $i_k(T(x))$

$$F_1(\tau_i) = \sum_{j=o}^{N-1} \frac{i_k(\tau_{j+1}) - i_k(\tau_j)}{\tau_{j+1} - \tau_j} (E_3(|\tau_i - \tau_j|) - E_3(|\tau_i - \tau_{j+1}|))$$

and the terms of the second order polynomial in the sublayers adjacent to x_i

$F_2(\tau_i) = 0$, if $\tau_i = 0$ or $\tau_i = \tau_0$, otherwise

$$\begin{aligned} F_2(\tau_i) = &\frac{2}{\tau_{i+1} - \tau_{i-1}} \left\{ \frac{i_k(\tau_{i+1}) - i_k(\tau_i)}{\tau_{i+1} - \tau_i} - \frac{i_k(\tau_i) - i_k(\tau_{i-1})}{\tau_i - \tau_{i-1}} \right\} \\ &\times \left\{ \tfrac{1}{3}(1 - \mathrm{e}^{-(\tau_i - \tau_{i-1})}) - \tfrac{1}{6}(\tau_i - \tau_{i-1}) \right. \\ &\times E_3(\tau_i - \tau_{i-1}) - \frac{\tau_i - \tau_{i-1}}{4} \\ &+ \tfrac{1}{3}(1 - \mathrm{e}^{-(\tau_{i+1} - \tau_i)}) - \tfrac{1}{6}(\tau_{i+1} - \tau_i) \\ &\left. \times E_3(\tau_{i+1} - \tau_i) - \frac{\tau_{i+1} - \tau_i}{4} \right\}. \end{aligned}$$

Radiative heat flux in band k [*see equation* (6)]

$$\begin{aligned} q_{\mathrm{rad},k}(x_i) = &2\pi \{n_k^2 (F_1^*(\tau_i) + F_2^*(\tau_i)) \\ &+ (i_k^+(0) - n_k^2 i_k(0)) \cdot E_3(\tau_i) \\ &- (\mathrm{i}_k^-(\tau_0) - \mathrm{n}_k^2 \mathrm{i}_k(\tau_0)) \cdot E_3(\tau_0 - \tau_i)\}, \end{aligned} \tag{A3}$$

with the terms of linear interpolation of $i_k(T(x))$ and with $\mathrm{sgn}(0) := -1$,

$$\begin{aligned} F_1^*(\tau_i) = &\sum_{j=0}^{N-1} \mathrm{sgn}(i-j) \frac{i_k(\tau_{j+1}) - i_k(\tau_j)}{\tau_{j+1} - \tau_j} \\ &\times (E_4(|\tau_i - \tau_j|) - E_4(|\tau_i - \tau_{j+1}|)) \end{aligned}$$

and the terms of second-order polynomial in the adjacent sublayers x_i

$F_2^*(\tau_i) = 0$, if $\tau_i = 0$ or $\tau_i = \tau_0$, otherwise

$$F_2^*(\tau_i) = \frac{2}{\tau_{i+1}-\tau_{i-1}}\left\{\frac{i_k(\tau_{i+1})-i_k(\tau_i)}{\tau_{i+1}-\tau_i} - \frac{i_k(\tau_i)-i_k(\tau_{i-1})}{\tau_i-\tau_{i-1}}\right\}$$
$$\times\left\{\tfrac{1}{4}(1-e^{-(\tau_i-\tau_{i-1})}) - \tfrac{1}{4}(\tau_i-\tau_{i-1})E_4(\tau_i-\tau_{i-1})\right.$$
$$-\frac{\tau_i-\tau_{i-1}}{6} - \tfrac{1}{4}(1-e^{-(\tau_{i+1}-\tau_i)}) + \tfrac{1}{4}(\tau_{i+1}-\tau_i)$$
$$\left.\times E_4(\tau_{i-1}-\tau_i) + \frac{\tau_{i+1}-\tau_i}{6}\right\}.$$

For an equally spaced grid ($\tau_{i+1}-\tau_i = \tau_i-\tau_{i-1}$) it is $F_2^*(x_i) = 0$.

Integrals in equation (5) *for the intensities at the boundaries*

$$\int_0^{\tau_0} i_k(T(\tau^*))\cdot E_2(\tau^*)\,d\tau^* = \tfrac{1}{2}i_k(0) - i_k(\tau_0)E_3(\tau_0) + \sum_{j=0}^{N-1} \times \frac{i_k(\tau_{j+1})-i_k(\tau_j)}{\tau_{j+1}-\tau_j}(E_4(\tau_j)-E_4(\tau_{j+1})), \quad \text{(A4)}$$

$$\int_0^{\tau_0} i_k(T(\tau^*))\cdot E_2(\tau_0-\tau^*)\,d\tau^* = \tfrac{1}{2}i_k(\tau_0) - i_k(0)E_3(\tau_0) + \sum_{j=0}^{N-1}\frac{i_k(\tau_{j+1})-i_k(\tau_j)}{\tau_{j+1}-\tau_j}(E_4(\tau_0-\tau_j)-E_4(\tau_0-\tau_{j+1})). \quad \text{(A5)}$$